IEEE Access
Multidisciplinary | Rapid Review | Open Access Journal

Received May 6, 2019, accepted June 2, 2019, date of publication June 5, 2019, date of current version June 19, 2019.

Digital Object Identifier 10.1109/ACCESS.2019.2921303

Sound Transmission-Based Elastography Imaging

DONGXU LIU[1], ZHIJIAN HU[1,2], GE WANG[3], (Fellow, IEEE), AND LIZHI SUN[1]

[1]Department of Civil and Environmental Engineering, University of California at Irvine, Irvine, CA 92697, USA
[2]School of Transportation, Wuhan University of Technology, Wuhan 430070, China
[3]Department of Biomedical Engineering, Rensselaer Polytechnic Institute, Troy, NY 12180, USA

Corresponding author: Lizhi Sun (lsun@uci.edu)

This work was supported by the US National Science Foundation under Grant CMMI-1229405.

ABSTRACT Elastography is of great interest in biomechanics and medical imaging due to its nondestructive capability of mapping elasticity of tissues. The elastography framework relies on external excitations which actuate deformation inside an object. The internal response is then acquired and analyzed to map the distribution of elastic moduli. In this paper, with no need of measuring any internal responses, an integrated elastography method is developed which only requires the transmitted responses of applied sound waves. During the process, the tomography image (e.g., CT or MRI) and the applied waves are integrated into a computational model. Following a procedure of inverse analysis, the elasticity of all phases in the object is reconstructed when the computational transmission of waves matches with the measured transmission. The numerical simulation on brain tissues and a demonstration on silicon rubber phantom are conducted to validate the proposed method. Both cases demonstrate that the integrated method successfully predicts the real elasticity of samples. The verification measurements on the phantom further show that the predicted elastic moduli agree well with the experimental results of uniaxial compression testing.

INDEX TERMS Elastography, elastic modulus, finite element method, sound wave, transmission.

I. INTRODUCTION

Elastography, as an emerging image modality, has drawn great attention due to its application prospect in characterizing biomechanical properties, which also is expected to strengthen the diagnosis of pathological changes and predict elasticity with the nondestructive mode [1]–[6]. It is well known that most cancerous or tumorous tissues are locally stiffer than their surroundings [7]. For example, most breast tumors confined to the ducts themselves are designated ductal carcinomas in situ (DCIS), which are the initial stage of malignant tumors. Pathological changes of these DCIS are known to be correlated with changes in tissue stiffness (modulus), resulting in extremely hard nodules. Masses form and grow because of inflammation and desmoplasia, a dense cellular reaction specific to malignant lesions with highly cross-linked collagenous fibers. In fact, the shear moduli of tissues vary over five orders of magnitude whereas other imaging modalities, CT, MRI and Ultrasound only detect tissues within two orders of magnitude as shown in Figure 1 of [8]. From this point of view, elastography is more promising in detecting cancerous tissues. Therefore, modulus-directed elastography has become an attractive tool to investigate the mechanical properties of tissues. Those mechanical parameters related to elasticity, including Young's modulus, shear modulus, strain, wave speed, and wave length, can be used to reconstruct elastography. To this end, an external excitation on tissues/phantoms, most commonly the sound wave including continuous and transient waves, is applied to measure these parameters inside tissues.

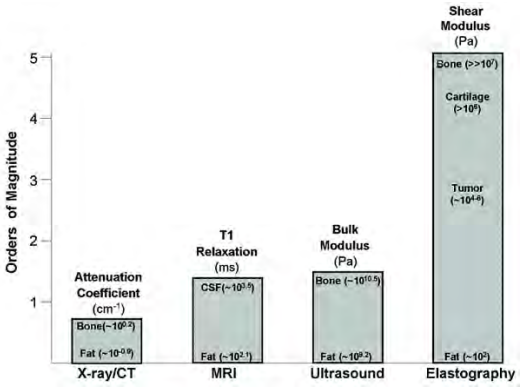

FIGURE 1. Imaging modality contrast mechanisms [8]. By comparison, elastography identifies the largest variation in resolving tissues.

The associate editor coordinating the review of this manuscript and approving it for publication was Yunjie Yang.

A great deal of research efforts working on elastography with sound waves and the commercial exploration for clinical application have been reported [9]–[16]. While a few anisotropic modeling works have been explored [4], [5], current efforts in the literature are dominantly in the assumption of isotropic elasticity, considering the tedious, time-consuming inverse computation and the focus on averaged identification of pathological changes. In the frame of linear elasticity some algorithms have been developed to map the elastography inversely, which are rooted in the governing equations of wave propagation in homogeneous isotropic elastic solid without the body force,

$$(\lambda + \mu)\, u_{j,ji} + \mu u_{i,jj} = \rho \ddot{u}_i \tag{1}$$

where λ and μ are Lamé constants (μ is also called the shear modulus), i and j are the coordinate indices ($i,\ j = 1, 2, 3$) in Cartesian tensor notation, u_j is the displacement vector, and ρ is the density of solid [17], [18]. By considering that the shear wave does not change volume, i.e., $u_{i,i} = 0$, the velocity of shear wave V_s can be derived as,

$$V_s = \sqrt{\mu/\rho} \tag{2}$$

As for continuous waves, after low-frequency shear waves are emitted into tissues by external sources, the local wavelengths are measured through either the color Doppler image or phase-contrast magnetic resonance image from which velocities are estimated and shear moduli are finally predicted based on (2) [1], [3], [19]. However, direct measurement is challenging because of irregular shapes and internal reflections of tissues. Therefore, by using (1), the model-based schemes, direct inversion and iterative inversion such as the elasticity tensor based reconstruction, the sub-zone based reconstruction, and the dynamic cardiac elastography, have been developed for continuous wave elastography [5], [17], [20], [21]. In addition, efforts coming from signal process and correlation analysis such as the reverberant shear-wave fields frame and the time reversal based reconstruction have been made to map continuous wave elastography [15], [22], [23]. As for transient waves, pulse shear waves are generated by external sources and deform tissues locally, which makes wavelengths or wave velocities measurable by tracking wave propagation such as shear wave elasticity imaging, supersonic shear imaging and shear wave speed imaging [24]–[26]. Overall, current elastography methods heavily rely on the internal mechanical responses to the external wave excitation. For example, the wavelength or the wave speed of the tissue needs to be detected to predict the elasticity distribution, in which critical problems remain to be solved, including overcoming wave attenuation in tissues, considering the reflection and refraction of wave at interfaces, random noise effect and sophisticated image processing [9]–[11], [14], [15], [17]. In elastodynamics, these mechanical responses are governed by the partial differential equation (1). In most of cases, however, tissues are of multiple phases and irregular shapes, which leads to difficulty finding analytical solutions to (1). Resultantly, computational methods as an effective means, most commonly, the finite element method (FEM), have been employed to solve (1).[5], [17], [21], [27]–[30].

In the article, an integrated method under the framework of isotropic elasticity, referred to as the sound transmission-based elastography, is proposed, using the tomography images (e.g., CT and MRI) and transmitted wave signals at surface locations. It is remarkable that only transmitted signals through the sample, not the internal responses inside the sample, are needed for the elastography reconstruction. The image and the wave incidence are integrated into a computational model. Following a procedure of inverse analysis, elasticity distribution of all phases in the object is reconstructed when the computational transmission converges to the measured transmission. The numerical simulation on brain tissues and the experiment on the silicon rubber phantom are conducted to validate the proposed method. Both cases illustrate that the integrated method successfully predicts the real elasticity of samples. The verification measurements on the phantom show the predicted elastic properties agree well with the experimental results of uniaxial compression testing.

The method and the corresponding validation and discussion are introduced in Sections II and III. The conclusions are in Section IV.

II. METHOD

Wave motion inside tissue media carries the information of the mechanical properties and so does its transmission carry the same information filtered by internal structures, which is completely controlled by the governing equations (1). The tomography image resolved by CT, MRI or Ultrasound contains the tissue structure information and can identify the position and size of suspicious lesions such as cancerous or tumorous tissues. They can be integrated and simulated in a computational model with FEM in which the wave incidence of sound test serves as the external load and the image is used to generate finite-element mesh. As for the elastic modulus of each phase in FEM, it is the goal that needs to be analyzed inversely and mapped. Thus, a computational model is built, and the elastography image is reconstructed following a procedure of inverse analysis when the FEM transmission output matches with the measured transmission signals at surface locations of object.

Specifically, the first step is to obtain the object tomography to characterize the internal structure. All tissues are segmented under CT/MRI resolution. The segmented tomography serves as the two-dimensional or three-dimensional geometry input of the inverse analysis as shown in Figure 2. The second step is to conduct the sound-wave test on the same object used in the first step. Sound transducers are laid out on the surface of the object, some of which serve as the emitters that fire the incident wave and others as the receivers that collect the transmitted signals. Depending on phases of a tissue that need to be mapped, the number of transducers should be enough for exciting each phase and receiving the transmission and reflection through each phase. The third step is to build a computational model based on the tomography

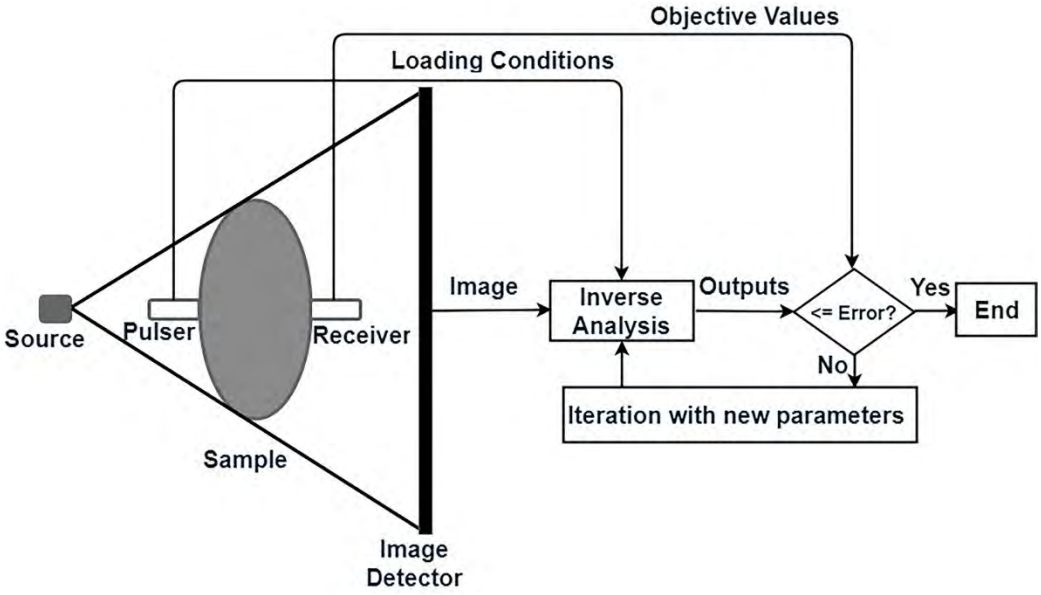

FIGURE 2. Flowchart of elastography based on tomography image and sound wave integration. The pulser and receiver are the sound-wave transducers. The cycle starts with image acquisition on the sample and ends with the match between the computational output and the objective value collected by the receiver.

image and the incident sound wave acted on the object. Image process may be necessary to convert image into a specific format acceptable for FEM meshing. The meshed regions are completely identical with segmented tissues in the first step. In this step, for the sake of ensuring accurate simulation, it is noted that there are at least 10 nodes representing each wavelength for whatever the element type (e.g., four-node quadrilateral elements, three-node triangular elements and 4-node tetrahedral elements) and the interpolation functions (e.g., second order shape functions) are adopted [31]. The displacement boundaries are set in terms of real conditions or without disturbing the real wave propagation when applying FEM. The fourth step is to conduct FEM simulation and inverse analysis until its output converges to measured transmission signals within the preset error as shown in Figure 2. As for the error, there is no general threshold available because the accuracy of inverse analysis is influenced by many factors such as signal noise, image noise, algorithms, numerical error, computation time, and so on. In practice, it could be determined empirically and be helpful to test the noise level in advance. The third and the fourth steps form a calculating loop in which the fourth one provides the parameter update for the third step.

Inversely mapping elastography is an optimization problem to find a set of variables making the objective function maximum or minimum. However, it is difficult to establish an explicit relationship between the transmitted signal and the elastic modulus. In physics, they are interrelated. In the study, the factorial design including the full factorial design and the orthogonal array design are employed to perform the inverse analysis [32], [33]. The design assembles all or part of possible combinations of optimization variables into an array of which the optimum values will be selected out, especially suitable for problems without explicit relationships between the objective value and corresponding optimization variables. Factorial design allows evaluating all variables' effect on the objective value in a single experiment (simulation). Currently, the variable and the objective function are bridged in the FEM simulations, following the factorial design. Based on the results of all simulations, the optimum values can be found. The full factorial design needs at least two factors (namely optimization variables), assigns possible values (also called levels) for each factor and, thereafter, executes calculations on all possible combinations of all levels across all factors. After those calculations are finished, the favorable levels can be optimized out by comparing with the objective value. If the number of calculations is so huge that the computation time is unacceptable, the orthogonal array design is another choice that doesn't need to exhaust every possibility across all factors and their levels, only considering selected possible combinations listed in an orthogonal array. These combinations of an orthogonal array are not assigned randomly, but following a strict rule so they can represent and cover all ones of every possibility [33]. It is noted that the value range (the upper and lower limits) of each factor needs to be preset, and otherwise the array cannot be designed for the factorial design. Fortunately, the reasonable elastic modulus ranges for most of biomaterials and tissues are predictive throughout the published literation and books.

III. VALIDATION

A. NUMERICAL VALIDATION

In this part, the integrated method is firstly demonstrated on a brain slice. The slice is an approximately 1-mm-

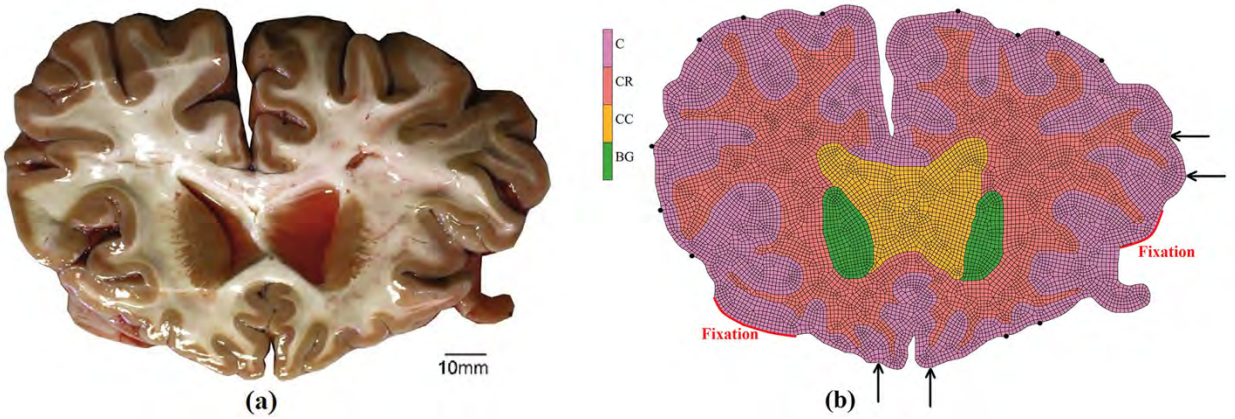

FIGURE 3. (a) The brain-tissue slice photograph and (b) the four regions meshed for FEM simulation, including the cortex (C), corona radiata (CR), corpus callosum (CC) and basal ganglia (BG). The four arrows show the incidence positions and the 12 black solid dots show the signal detection locations. The 'Fixation' boundaries marked by red curves mean that displacement is constrained to be zero during FEM simulation.

thick corona and cut off from a cadaver as photographed in Figure 3 (a) [34]. The photograph is formatted to TIFF files and imported into *Simpleware ScanIP* (Synopsys, Inc.) for segmentation. With the pixel intensity-based segmentation, the interfaces among different functional tissues are identified. It is then transformed into two-dimensional FEM meshes with four regions. Following the names and positions of tissues [34], the four regions are the cortex (C), corona radiata (CR), corpus callosum (CC) and basal ganglia (BG) as shown in Figure 3 (b). Brain ventricles are currently treated as CC.

Numerical model creation and simulation are conducted on the commercial FEM package, *Marc Mentat 2018.0.0* (MSC Software Corporation), with the assist of a Python script performing the factorial design, the parameter update and mathematical process. The model is meshed into 11261 four-node quadrilateral elements. The incident wave is the 50 Hz sine signal applied at four positions on the outer boundary denoted by arrows in Figure 3 (b). As denoted by the black sold dots in Figure 3 (b), twelve locations are chosen to detect the transmission with the sample rate of 400/s. The acquisition duration is 0.2 s. All tissues in this study are treated as linear elasticity for demonstrating the integrated method first on linear materials. The set of shear moduli, [C = 1.43, CR = 0.66, CC = 0.35, BG = 0.70] kPa, reported by Budday et al. (2017) is used as the objective values and the corresponding output at 12 locations as the objective signals. Accordingly, the elastic moduli are [4.26, 1.97, 1.04, 2.09] kPa if Poisson's ratio of 0.49 is assumed for all tissues. The density is assumed 1000 kg/m^3. In this case, full factorial design is employed to recognize the optimality for all levels of factors. So, there are four factors corresponding to elastic moduli of C, CR, CC and BG. In terms of the reasonable ranges of their moduli, 3.0 kPa $\sim$ 6.0 kPa for region C and 0.1 kPa $\sim$ 3.0 kPa for other three regions, each factor is assigned eight levels at first, [3.0, 3.4, 3.8, 4.2, 4.6, 5.0, 5.4, 6.0] kPa for C and [0.1, 0.5, 0.9, 1.3, 1.7, 2.1, 2.5, 3.0] for others. Totally, it is 8^4 (4096) trials for possible combinations of all levels. Running on a PC with Intel(R) Core(TM) i7-3770 CPU @ 3.40GHz and 16.0 GB RAM, each trial takes 21 seconds. From this point of view, the computation of current inverse analysis is acceptable and effective. Because cross-correlation can be used to observe the similarity of two signals [35], the objective function will be established based on the cross-correlation of the objective signals and each trial ones. The maximum of cross-correlation is at the zero lag time if two signals are identical, which is so-called auto-correlation. For this case, the objective function of the optimization problem is defined as

$$\begin{aligned} \min f(\boldsymbol{E}) &= \sqrt{\sum_{i=1}^{12}\left(1-\frac{D_C^i|_{t=0}}{D_A^i|_{t=0}}\right)^2} \\ \textit{Subject to}: \quad & \min f(\boldsymbol{E}) \le 1.0\% \end{aligned} \tag{3}$$

where $\boldsymbol{E} = (E_C, E_{CR}, E_{CC}, E_{BG})$, standing for the elastic moduli attempt in each level, $D_A^i|_{t=0}$ is the auto-correlation of the measured signals of point i at the zero lag time, and $D_C^i|_{t=0}$ is the cross-correlation of the trial signals and the measured signals of point i at the zero lag time. The effect of $\boldsymbol{E}$ on $D_C^i|_{t=0}$ is implicit in (3). But, they are bridged in FEM in which $\boldsymbol{E}$ are the material parameter input and $D_C^i|_{t=0}$ is determined according to FEM output. The measured signals that are the objective signals come from the FEM simulation with the objective elastic moduli of [4.26, 1.97, 1.04, 2.09] kPa. Applying (3) to 4096 trials, $min\, f(\boldsymbol{E})$ is reached at [4.2, 2.1, 0.9, 2.1] kPa of the 2732nd trial, meaning that the 2732nd one is the closest to real values among all trials. However, the error of the trial is 4.3%, larger than 1.0%. In practice, 4.3% could be enough for mapping elasticity. As an illustration for three surface locations, the objective signals of the displacement amplitude and the corresponding simulation signals of the best trial 2732 are plotted in Figure 4 (a). By contrast, there is discrepancy for some locations between two set of signals, which causes the 4.3% error. For presenting the more accurate solution, the inverse analysis is continued until meeting $min\, f(\boldsymbol{E}) \le 1.0\%$.

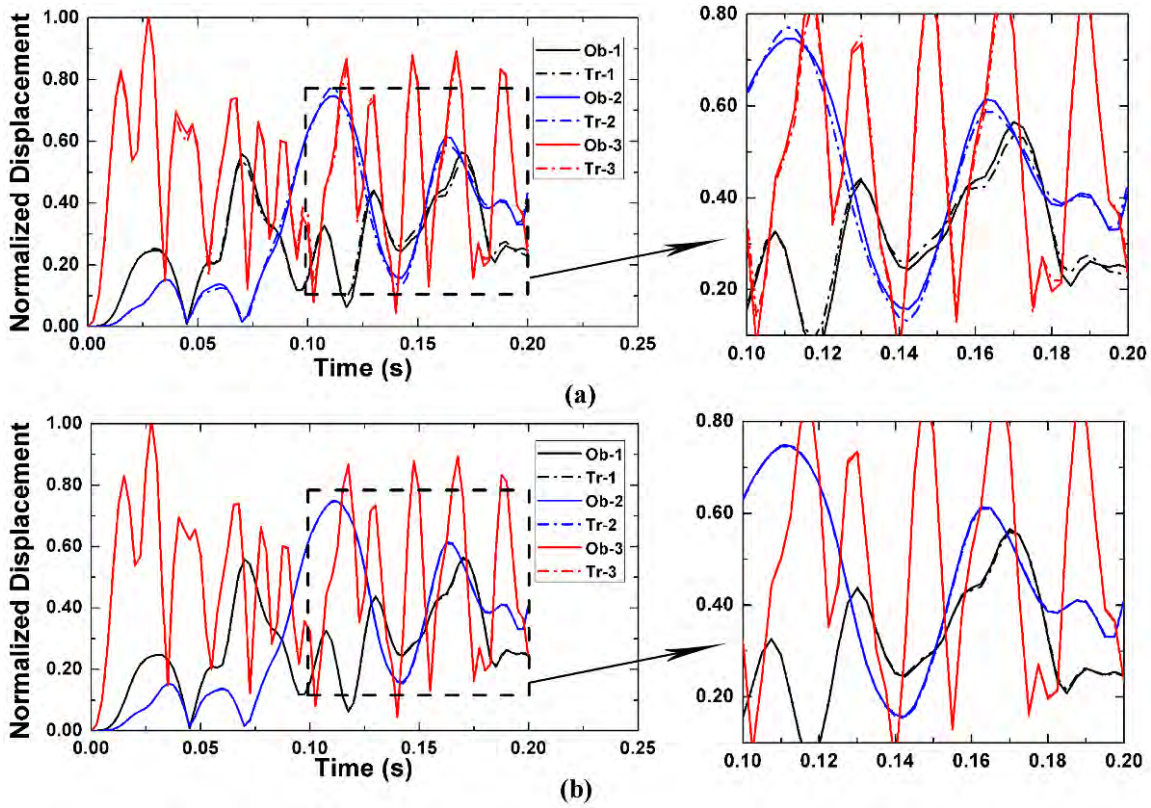

FIGURE 4. (a) The comparison of the target signals and the best trial ones in the first round and (b) the comparison of the target signals and the best trial ones in the fourth round. 'Ob' stands for the target signals and 'Tr' for the output ones from the best trial.

The first-round design helps to compress the value ranges for the further design. As a result, based on each value in [4.2, 2.1, 0.9, 2.1] kPa of the first-round, next round factorial design, with the smaller step, sets [3.90, 4.05, 4.20, 4.35, 4.50] for C, [1.80, 1.95, 2.10, 2.25, 2.40] for CR, [0.60, 0.75, 0.90, 1.05, 1.20] for CC and [1.80, 1.95, 2.10, 2.25, 2.40] for BG, which introduces 625 trials. This round ends up with [4.20, 2.10, 1.05, 2.10]. Because the result is almost same as that of the first-round, the step of levels is needed to be furtherly decreased. Levels of the third round are set to [4.10, 4.15, 4.20, 4.25, 4.30] for C, [2.00, 2.05, 2.10,C 2.15, 2.20] for CR, [0.80, 0.85, 0.90, 0.95, 1.00] for CC and [1.85, 1.90, 1.95, 2.00, 2.05] for BG. After all trials are completed, the third round gives [4.25, 2.00, 1.00, 2.05] with 4.1%. Once more, the level range of the fourth round is narrowed down with the much smaller step, [4.23, 4.25, 4.27] for C, [1.98, 2.00, 2.02] for CR, [0.98, 1.00, 1.02] for CC and [2.03, 2.05, 2.07] for BG. Eventually, [4.27, 1.98, 1.02, 2.07] is finalized as the optimum trial with 1.0%. The comparison of the objective signals and the corresponding ones of the best trial is plotted in Figure 4 (b) for the same locations as in Figure 4 (a). The two set of signals are almost overlapping, which illustrates again [4.27, 1.98, 1.02, 2.07] are the optimum values, consistent with real elastic moduli of [4.26, 1.97, 1.04, 2.09] with errors 0.2%, 0.5%, 1.9% and 1.0%, respectively. In the whole course, any internal information is not detected and processed to map the moduli.

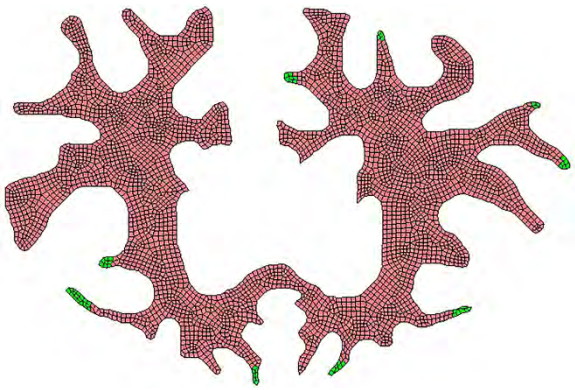

FIGURE 5. 1.3% of CR, colored by green, is segmented into C and all corresponding properties are also set as same as those of C.

All information for the mapping is based on signals on the 12 surface locations.

The current study maps stiffness on segmented tomography image. For demonstrating the sensitivity to segmentation, 1.3% of CR assumed as the segmentation error is artificially merged into C as shown in Figure 5. After analysis, the merging will introduce the 4.1% error by using (3), showing that this study has the good sensitivity to segmentation.

In real case, the brain is enclosed by a skull that may make the wave transmission too weak to be caught. However, the skull is not completely closed, having outlets such as nose,

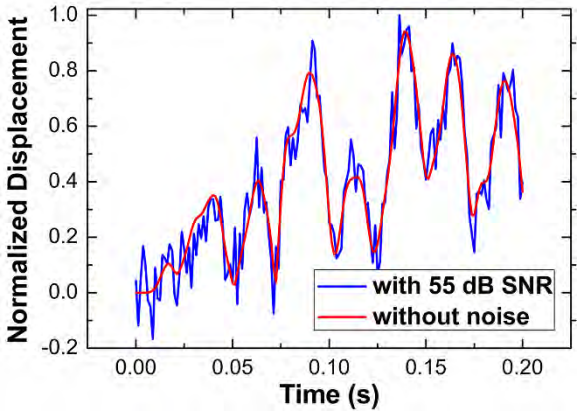

FIGURE 6. A typical output under the 100 Hz sine incidence: Without noise and with the SNR of 55 dB.

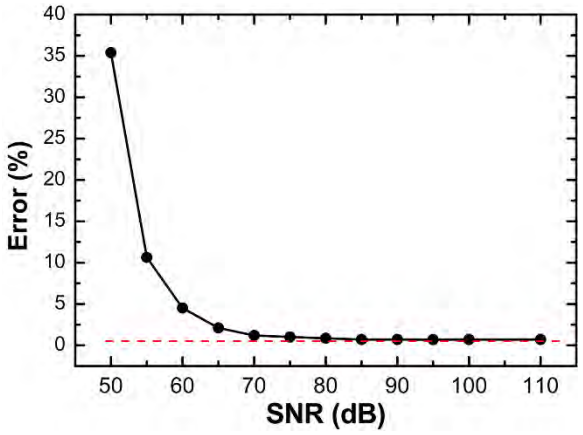

FIGURE 7. Errors with different SNR values and the dash line showing the 0.7% position.

mouth, eye, ear, and neck regions. The receivers can be placed around these regions to collect transmission.

It is noticed that the sound incidence is compressional waves. But, current study also applies to shear waves for it does not need to track and measure any internal signal, but its transmission. One of main reasons making shear wave elastography the most popular method is that speeds of compressional waves are so high that they are difficult to be tracked [36]. For the current study, there are no frequency limits because it does not need to adjust frequencies to make the wavelength measurable and trackable. However, specific frequency should be selected to make sure that the transmitted signals can be detected. For example, if the incident wave is changed to 100 Hz, following the same process of the 50 Hz analysis, it still ends at [4.27, 1.98, 1.02, 2.07] with 0.7% error. In order to basically understand the effect of signal-to-noise ratio (SNR), the measured signals that are the output under the real set of moduli are added artificially with white Gaussian noise. Figure 6 shows a typical output of one location without noise and its corresponding signals with 55 dB SNR. Different SNR values are tried and analyzed from 50 dB to 110 dB. With the SNR increase, the error decreases quickly and approaches 0.7% as shown in Figure 7. It can be seen that the SNR be at least up to 55 dB for having a reasonable estimation. Therefore, in practice, frequency needs to be chosen for having an enough SNR. Furthermore, the 1.0% error in (3) could be too strict because of noise in reality. For this case, if the noise level is at the SNR of 60 dB, the error is about 5%.

B. EXPERIMENTAL VALIDATION

1) PHANTOM PREPARATION

The phantom consists of the silicone rubber being the matrix and a piece of vinyl polymer being the inclusion. There are five procedures in manufacturing the phantom. First, the required amount of silicone base is poured into a plastic beaker. Second, the curing agent is added. Third, the components are thoroughly mixed by a *Caframo*^{TM} mechanical stirrer for 20 minutes at a rotation speed of 280 rpm. The viscous media is further degassed in a vacuum for 30 minutes in order to eliminate the air bubbles trapped in the mixture. Finally, as soon as no air bubbles puff from the top surface, the polymer inclusion is dropped in. The sample in shape of the conical frustum is made after curing at room temperature for 6 days as shown in Figure 8.

2) APPLICATION OF THE INTEGRATED METHOD

The achievement of the integrated method resides in the sample spatial structure, sound-wave test, FEM modeling and inverse analysis as stated in Section II. Because of irregularity of the inclusion geometry, its 3D image is imaged by an X-ray CT scanner, *Xradia 410 Versa* (Carl Zeiss X-ray Microscopy, Inc.) as shown in Figure 8. The 0.4X lens with the voxel size of 25 micrometers is used to scan the inclusion. With the sample rotation step of 0.225°, 1600 projections are acquired to reconstruct the 3D image. After scanning, the commercial image process software, *Simpleware ScanIP* (Synopsys, Inc.), steps in to segment based on each pixel intensity and convert X-ray CT image to a compatible format that can be imported into *Marc Mentat*.

Next is to have the sound-wave tested on the sample to acquire the transmitted signals. The sound testing system is two *R3α* transducers and one *FieldCal AE Signal Generator* (MISTRAS Group, Inc.). The operation frequency range of R3α is 25 kHz $\sim$ 70 kHz. One of transducers functions as the pulser while another one as the receiver. In the test, the incident wave is a 30 kHz sine tone burst with the peak value of 4467 Pa and 1 ms duration which is emitted by the Generator. A silicon-based lubricant is coated on sample areas on which transducers are placed. Two transducers are positioned coaxially, making waves passing through both matrix and inclusion, as shown in Figure 9. During the test, the transmitted peak acquired by the receiver is 22.4 Pa that will be used later as the objective value of the inverse analysis.

The third step is to build the computational model with *Marc Mentat*. The inclusion image scanned by Nano CT is imported into *Marc Mentat*. Because the matrix is regular, it is drawn directly by *Marc Mentat*. Both matrix and inclusion are

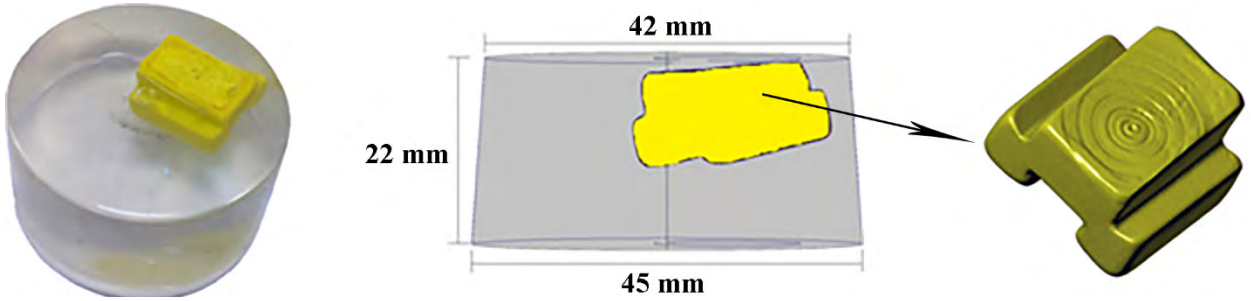

FIGURE 8. Left: The phantom of silicone matrix and polymeric inclusion, Middle: Main dimensions, and right: 3D inclusion image resolved by X-ray CT.

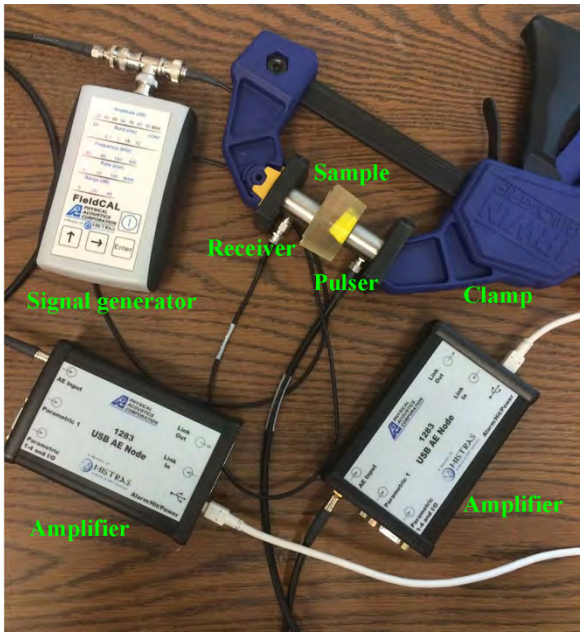

FIGURE 9. Sound test on the sample. One transducer serves as the pulser and the other serves as the receiver. The incidence of a 30 kHz sine tone burst is generated by the signal generator.

treated as elastic materials. The loading condition is set on the position in which the incident wave is emitted by the *R3α* transducer. The whole 3D model is meshed into 89585 four-node tetrahedral elements. During the simulation, a point on the intersection of the bigger top surface and the side surface is fixed as the displacement boundary during FEM simulation.

In fact, there should be wave reflection at interface between the sample and the lubricant due to impedance mismatch. Wave undergoes two times reflection before it passes through the sample. One is on the incident interface and another on the emergent interface. The final transmission is affected by the two reflection and has a connection with the signal amplitude and material properties. At this point, FEM simulation needs to take reflection into account as following,

$$P_t = TP_0 \tag{4}$$

$$T = \frac{2Z_2}{Z_1 + Z_2} \tag{5}$$

where P_0 is the incident pressure emitted directly from the transducer, P_t is the transmitted pressure, T is the transmission coefficient defined as the fraction of the incident pressure, Z is the acoustic impedance that is the product of density and sound wave speed, and the subscripts 1 and 2 represent media proximal and distal to the interface [37].

The last step is to conduct inverse analysis. In the case, six factors are designed: moduli, Poisson's ratio and density of both matrix and inclusion. If five levels are associated with each factor, the full factorial design needs totally 5^6 (15625) trials, which is time-consuming in computation. In order to reduce the number of trials, an orthogonal array is specifically designed to investigate this inverse analysis. As for the six 5-level factors, there are 25 trials according to the principle of the orthogonal array design [33]. Mathematically, the 25 trials can represent 15625 ones of the full factorial design. It must be kept in mind that the transmission coefficient of every trial should be updated with (5). The amplitude of incident wave into the sample keeps updating with (4) as well for each trial during FEM simulating. In the 3D simulation, each trial takes 4 minutes, meaning 100 minutes for total 25 trials. From this point of view, the computation of current inverse analysis is acceptable and effective. Likewise, the orthogonal design needs the possible range of each factor value that will be narrowed down since the initial rough estimation. The finalized levels of each factor are listed in TABLE 1. In the column 'Factors', 1, 2 and 3 denote the modulus, the Poisson's and the density of matrix, respectively, and 4, 5 and 6 denote the modulus, the Poisson's and the density of inclusion, respectively. After the 25 trials are finished, the difference between the peak pressure of FEM output and the experimental peak (22.4 Pa) is calculated for each trial. Then, the difference is classified by levels for each factor and averaged over the number of levels as shown in Figure 10 from which the optimum levels corresponding to the minimum average can be read out directly: modulus of 2.0 MPa, Poisson's ratio of 0.30 and density of 1050∼1150 kg/m^3 for matrix, and 2.6 MPa, 0.39 and 1600∼1700 kg/m^3 for inclusion. The density is given in a range, illustrating that the objective value is not sensitive to density variation in contrast with other factors. Figure 11 shows the computational output of the optimum levels which gives the peak of 21.5 Pa, matching well with the measured value of 22.4 Pa with the 4.0% error.

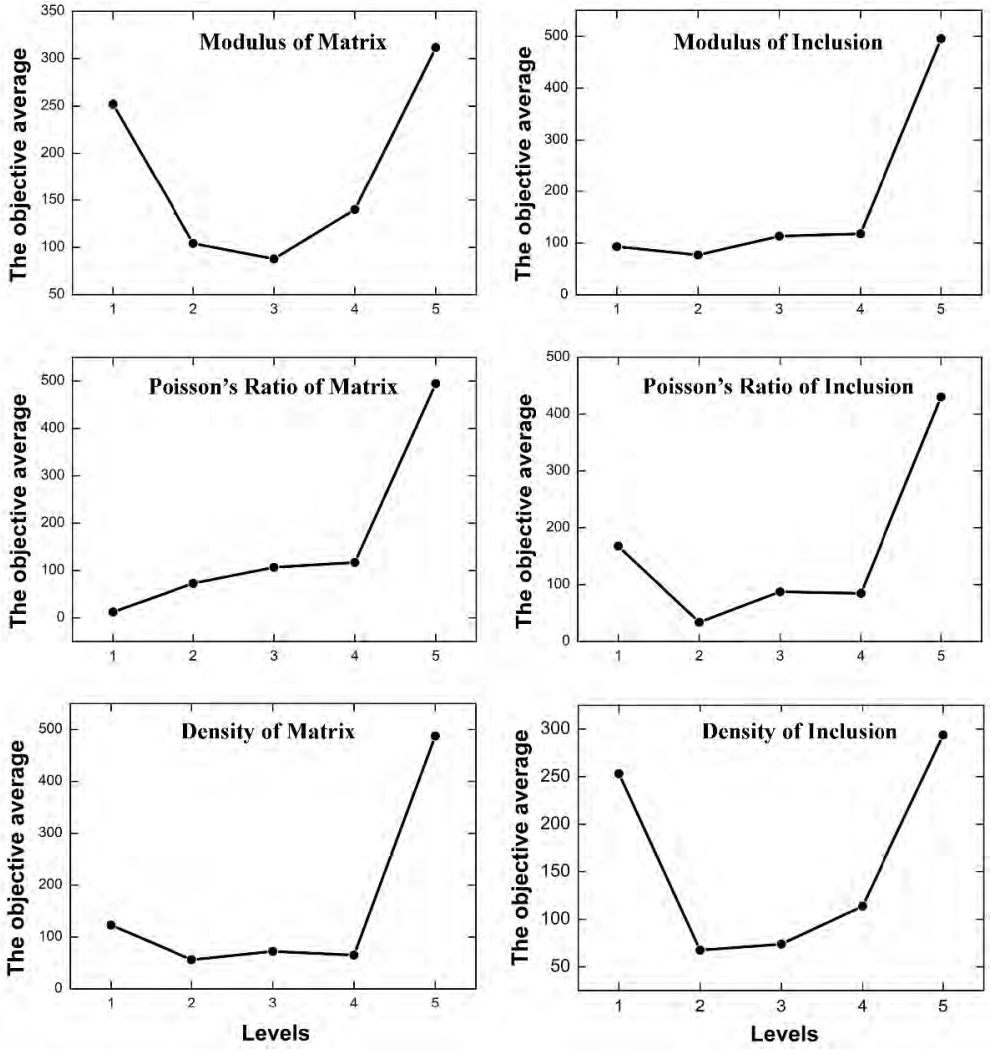

FIGURE 10. The FEM output average of each level of every factor: x-coordinate is the level number for each factor, and y-coordinate is the output average corresponding to each level. The level holding the minimum average is optimum.

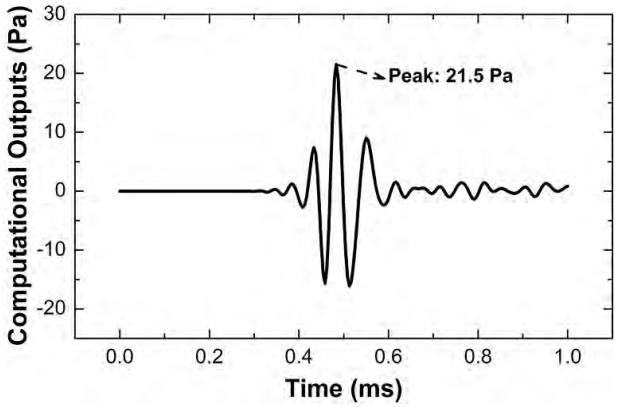

FIGURE 11. The FEM pressure output with optimum values: Modulus of 2.0 MPa, Poisson's ratio of 0.30 and density of 1050 kg/m3 for matrix, and 2.6 MPa, 0.39 and 1600 kg/m3 for inclusion.

With numerical errors and measurement noises, 4.0% may be considered good match.

Although the integrated method has completely been applied to the phantom and those unknown properties obtained, there still is a doubt whether those optimum values are real. For further verifying the method and the optimization, in next part, some of properties are measured experimentally.

3) VERIFICATION OF THE OPTIMIZATION

The density and moduli of matrix and inclusion are measured for the verification. The mass is tested directly by a balance and the volume by a graduated cylinder and water. The volume is the difference of the two readouts of water surface positions before and after the matrix or inclusion is put in the cylinder. At last, the density of matrix is 1050 kg/m^3, and the density of inclusion is 1690 kg/m^3. Both values are all in the optimization range of density, meaning that their optimum values agree with measurements.

The modulus is measured through the uniaxial compression by the tester, *BOSE ElectroForce® 3200*. The sample for matrix is a cylinder of 9.7 mm × 9.6 mm, and the sample for the polymer inclusion is a cuboid of 11 mm × 9.4 mm × 5.7 mm. The compression speed is

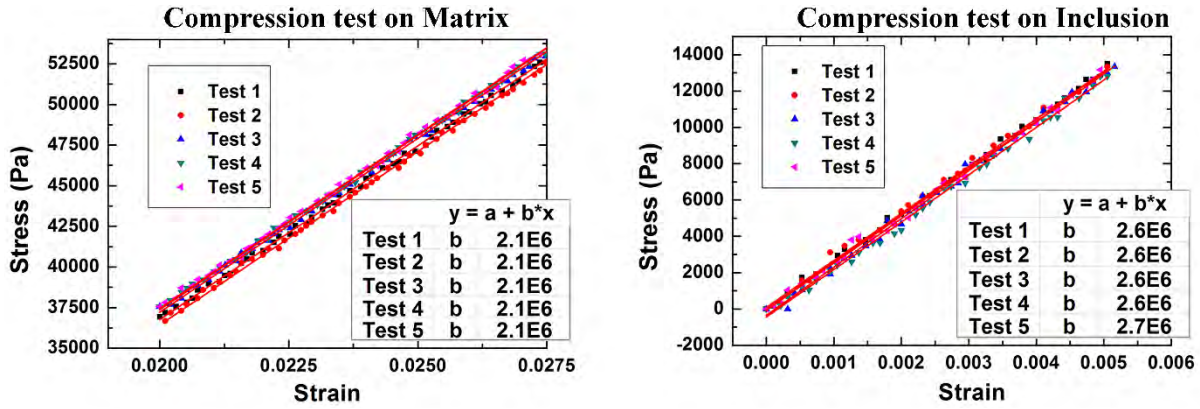

FIGURE 12. Compression stress-strain curves and their linear fits: the slopes are the moduli. All of five tests on each sample show good repeats.

TABLE 1. Levels for six factors.

Factors	Levels				
	1	2	3	4	5
1	1.2	1.6	2.0	2.4	2.8
2	0.30	0.35	0.40	0.45	0.49
3	1000	1050	1100	1150	1200
4	2.2	2.6	3.0	3.4	3.8
5	0.35	0.39	0.43	0.47	0.49
6	1500	1600	1700	1800	1900

0.01 mm/s under the displacement control. Five tests are conducted for each sample, and then followed by the linear fit on stress-strain curves as shown in Figure 12. The slopes are the moduli: 2.1 MPa for matrix and 2.6 MPa for inclusion. By comparison, the optimum values of 2.0 MPa and 2.6 MPa are consistent with the measured moduli for matrix and inclusion, respectively.

Overall, as demonstrated on the 2D case and the 3D phantom, the integrated method can predict the accurate elasticity. Because the objective value is not built as the explicit function of variables, factorial design provides a way making the inverse analysis effective and controllable. It is also noted that the current investigation is limited under the assumption of isotropic elasticity of tissues. Future work is needed to extend the method for general anisotropic elastography.

IV. CONCLUSION

A sound transmission-based elastography method is developed, which is validated on 2D and 3D cases with different waveform input and frequencies. This method can potentially be an effective tool in both fields of charactering elasticity of biomaterials/tissues and engineering materials. While the experimental validation of the method uses X-ray tomography image, other imaging modalities may work as long as they can provide the geometric delineation. One of the unique features of the current study is that no interior responses within objects, such as displacement, strain, or wave speed, need to be measured in advance for mapping elastography. At this standpoint, samples act as a "black-box" which also makes the experimental measurement free of considering the reflection and the refraction inside the object. Another feature is that the tomography image containing the geometric structures and sound wave carrying the material properties are integrated into FEM in which sound wave test is simulated and analyzed inversely to map the mechanical properties. Fundamentally, the current method is free of the frequency effect because it doesn't need to adjust the frequency to make internal responses trackable and measurable. Simulations and phantom experiments have been conducted to validate the proposed integrated method. The optimum results of density and moduli have been verified with the experimental measurements.

REFERENCES

[1] R. M. Lerner, S. R. Huang, and K. J. Parker, ""Sonoelasticity" images derived from ultrasound signals in mechanically vibrated tissues," *Ultrasound Med. Biol.*, vol. 16, no. 3, pp. 231–239, Jan. 1990.

[2] J. Ophir, I. Céspedes, H. Ponnekanti, Y. Yazdi, and X. Li, "Elastography: A quantitative method for imaging the elasticity of biological tissues," *Ultrasonund Imag.*, vol. 13, no. 2, pp. 111–134, Apr. 1991.

[3] R. Muthupillai, D. J. Lomas, P. J. Rossman, J. F. Greenleaf, A. Manduca, and R. L. Ehman, "Magnetic resonance elastography by direct visualization of propagating acoustic strain waves," *Science*, vol. 269, no. 5232, pp. 1854–1857, 1995.

[4] Y. Liu, L. Z. Sun, and G. Wang, "Tomography-based 3-D anisotropic elastography using boundary measurements," *IEEE Trans. Med. Imag.*, vol. 24, no. 10, pp. 1323–1333, Oct. 2005.

[5] Y. Liu, G. Wang, and L. Z. Sun, "Anisotropic elastography for local passive properties and active contractility of myocardium from dynamic heart imaging sequence," *Int. J. Biomed. Imag.*, vol. 2006, 2006, Art. no. 45957.

[6] Y.-L. Liu, D. Liu, L. Xu, C. Su, G.-Y. Li, L.-X. Qian, and Y. Cao, "*In vivo* and *ex vivo* elastic properties of brain tissues measured with ultrasound elastography," *J. Mech. Behav. Biomed. Mater.*, vol. 83, pp. 120–125, Jul. 2018.

[7] F. A. Duck, *Physical Properties of Tissue: A Comprehensive Reference Book*. New York, NY, USA: Academic, 1990.

[8] Y. K. Mariappan, K. J. Glaser, and R. L. Ehman, "Magnetic resonance elastography: A review," *Clin. Anatomy*, vol. 23, no. 5, pp. 497–511, Jul. 2010.

[9] K. J. Parker, M. M. Doyley, and D. J. Rubens, "Imaging the elastic properties of tissue: The 20 year perspective," *Phys. Med. Biol.*, vol. 57, no. 1, pp. 5359–5360, Jan. 2012.

[10] R. J. DeWall, "Ultrasound elastography: Principles, techniques, and clinical applications," *Crit. Rev. Biomed. Eng.*, vol. 41, no. 1, pp. 1–19, 2013.

[11] U. Zaleska-Dorobisz, K. Kaczorowski, A. Pawluś, A. Puchalska, and M. Inglot, "Ultrasound elastography—Review of techniques and its clinical applications," *Adv. Clin. Exp. Med.*, vol. 23, no. 4, pp. 645–655, Jul./Aug. 2014.

[12] T. Shiina, "Ultrasound elastography: Development of novel technologies and standardization," *Jpn. J. Appl. Phys.*, vol. 53, no. 7, 2014, Art. no. 07KA02.
[13] R. M. Sigrist, J. Liau, A. El Kaffas, M. C. Chammas, and J. K. Willmann, "Ultrasound elastography: Review of techniques and clinical applications," *Theranostics*, vol. 7, no. 5, pp. 1303–1329, 2017.
[14] T. J. Hamilton, C. J. Bailat, S. Gehring, C. Laperle, J. Wands, C. Rose-Petruck, and G. J. Diebold, "X-ray elastography: Modification of X-ray phase contrast images using ultrasonic radiation pressure," *J. Appl. Phys.*, vol. 105, no. 10, May 2009, Art. no. 102001.
[15] K. J. Parker, J. Ormachea, F. Zvietcovich, and B. Castaneda, "Reverberant shear wave fields and estimation of tissue properties," *Phys. Med. Biol.*, vol. 62, no. 3, pp. 1046–1061, Feb. 2017.
[16] J. Racedo and M. W. Urban, "Evaluation of reconstruction parameters for 2-D comb-push ultrasound shear wave elastography," *IEEE Trans. Ultrason., Ferroelectr., Freq. Control*, vol. 66, no. 2, pp. 254–263, Feb. 2018.
[17] M. M. Doyley, "Model-based elastography: A survey of approaches to the inverse elasticity problem," *Phys. Med. Biol.*, vol. 57, no. 3, pp. R35–R73, Feb. 2012.
[18] K. F. Graff, *Wave Motion in Elastic Solids*. New York, NY, USA: Dover, 1991.
[19] J. B. Weaver, E. E. W. Van Houten, M. I. Miga, F. E. Kennedy, and K. D. Paulsen, "Magnetic resonance elastography using 3D gradient echo measurements of steady-state motion," *Med. Phys.*, vol. 28, no. 8, pp. 1620–1628, Aug. 2001.
[20] R. Sinkus, J. Lorenzen, D. Schrader, M. Lorenzen, M. Dargatz, and D. Holz, "High-resolution tensor MR elastography for breast tumour detection," *Phys. Med. Biol.*, vol. 45, no. 6, pp. 1649–1664, Jun. 2000.
[21] E. E. W. Van Houten, M. I. Miga, J. B. Weaver, F. E. Kennedy, and K. D. Paulsen, "Three-dimensional subzone-based reconstruction algorithm for MR elastography," *Magn. Reson. Med.*, vol. 45, pp. 827–837, May 2001.
[22] S. Catheline, N. Benech, J. Brum, and C. Negreira, "Time reversal of elastic waves in soft solids," *Phys. Rev. Lett.*, vol. 100, no. 6, Feb. 2008, Art. no. 064301.
[23] J. Brum, S. Catheline, N. Benech, and C. Negreira, "Quantitative shear elasticity imaging from a complex elastic wavefield in soft solids with application to passive elastography," *IEEE Trans. Ultrason. Ferroelectr. Freq. Control*, vol. 62, no. 4, pp. 673–685, Apr. 2015.
[24] A. P. Sarvazyan, O. V. Rudenko, S. D. Swanson, J. B. Fowlkes, and S. Y. Emelianov, "Shear wave elasticity imaging: A new ultrasonic technology of medical diagnostics," *Ultrasound Med. Biol.*, vol. 24, no. 9, pp. 1419–1435, Dec. 1998.
[25] J. Bercoff, M. Tanter, and M. Fink, "Supersonic shear imaging: A new technique for soft tissue elasticity mapping," *IEEE Trans. Ultrason., Ferroelectr., Freq. Control*, vol. 51, no. 4, pp. 396–409, Apr. 2004.
[26] L. Ji, J. R. McLaughlin, D. Renzi, and J.-R. Yoon, "Interior elastodynamics inverse problems: Shear wave speed reconstruction in transient elastography," *Inverse Problems*, vol. 19, no. 6, pp. S1–S29, Dec. 2003.
[27] K. J. Parker, S. R. Huang, R. A. Musulin, and R. M. Lerner, "Tissue response to mechanical vibrations for "sonoelasticity imaging," *Ultrasound Med. Biol.*, vol. 16, no. 3, pp. 241–246, Jan. 1990.
[28] Y. Liu, G. Wang, and L. Z. Sun, "Elastography method to identify material distribution in two-phase nonlinear media," *J. Eng. Mech.*, vol. 140, no. 5, 2014, Art. no. 04014010.
[29] Z. Yuan, H. Zhao, C. Wu, Q. Zhang, and H. Jiang, "Finite-element-based photoacoustic tomography: Phantom and chicken bone experiments," *Appl. Opt.*, vol. 45, no. 13, pp. 3177–3183, May 2006.
[30] T. Kitazaki, K. Kondo, M. Yamakawa, and T. Shiina, "Shear wavelength estimation based on inverse filtering and multiple-point shear wave generation," *Jpn. J. Appl. Phys*, vol. 55, Jun. 2016, Art. no. 07KF10.
[31] F. J. Serón, F. J. Sanz, M. Kindelán, and J. I. Badal, "Finite-element method for elastic wave propagation," *Commun. Appl. Numer. Methods*, vol. 6, no. 5, pp. 359–368, Jul. 1990.
[32] D. C. Montgomery, *Design And Analysis Of Experiments*, 5th ed. Hoboken, NJ, USA: Wiley, 2000.
[33] P. J. Ross, *Taguchi Techniques for Quality Engineering*, 2nd ed. New York, NY, USA: McGraw-Hill, 1996.
[34] S. Budday, G. Sommer, C. Birkl, C. Langkammer, J. Haybaeck, J. Kohnert, M. Bauer, F. Paulsen, P. Steinmann, E. Kuhl, and G. A. Holzapfel, "Mechanical characterization of human brain tissue," *Acta Biomater.*, vol. 48, pp. 319–340, Jan. 2017.
[35] K. J. Keesman, *System Identification: An Introduction*. London, U.K.: Springer, 2011.
[36] B. S. Garra, "Elastography: History, principles, and technique comparison," *Abdominal Imag.*, vol. 40, no. 4, pp. 680–697, Apr. 2015.
[37] J. T. Bushberg, J. A. Seibert, E. M. Leidholdt, Jr., J. M. Boone, C. W. Mitchell, R. Shaw, A. Jackson, and B. Rivera, *The Essential Physics of Medical Imaging*, 3rd ed. Philadelphia, PA, USA: Lippincott Williams & Wilkins, 2012.

DONGXU LIU received the bachelor's degree in civil engineering, China, in 2001, and the master's degree in mechanical engineering from the Institute of Mechanics, Chinese Academy of Sciences, in 2004. He is currently pursuing the Ph.D. degree with the Department of Civil and Environmental Engineering, University of California at Irvine. His research interests include the methodology and algorithm of elastography, and the investigation of concrete properties based on elastodynamics and computational micromechanics.

ZHIJIAN HU received the Ph.D. degree in bridge and tunnel engineering from Tongji University, Shanghai, China, in 2006. He is currently a Professor with the Department of Road and Bridge Engineering, Wuhan University of Technology, China. He served as a Visiting Scholar at University of California at Irvine, from 2013 to 2014. He has published more than 50 papers in the fields of structural mechanics and bridge engineering. His main research interest includes composite materials and their application in civil engineering.

GE WANG is currently a Clark & Crossan Endowed Chair Professor and the Director of the Biomedical Imaging Center, Rensselaer Polytechnic Institute, Troy, NY, USA. He authored the pioneering paper on the first spiral/helical cone-beam/multi-slice CT algorithm, in 1991. Currently, there are over 100 million medical CT scans yearly with a majority in the spiral/helical cone-beam/multi-slice mode. His research results are featured in Nature, Science, and PNAS, and recognized with academic awards. He authored over 450 peer-reviewed journal publications, receiving a high number of citations. His interest includes x-ray CT, MRI, optical molecular tomography, multimodality fusion, and machine learning for medical imaging. He is the Lead Guest Editor of the five IEEE TRANSACTIONS ON MEDICAL IMAGING Special Issues, the founding Editor-in-Chief of the *International Journal of Biomedical Imaging*, and an Associate Editor of the IEEE TRANSACTIONS MEDICAL IMAGING, IEEE ACCESS, the IEEE TRANSATIONS ON RADIATION AND PLASMA MEDICAL SCIENCES, *Medical Physics*, and other journals. He is Fellow of the SPIE, OSA, AIMBE, AAPM, and AAAS.

LIZHI SUN received the Ph.D. degree in structural mechanics from the University of California –Los Angeles (UCLA), in 1998. He is currently a Professor with the Department of Civil and Environmental Engineering, University of California at Irvine (UCI). His main area of research interest is the micromechanics of heterogeneous composite materials, with applications for civil, mechanical, aerospace, and biomedical engineering. He has published more than 100 journal papers in the fields of mechanics and materials, applied physics, and biomedical engineering. He is an Editor of *International Journal of Damage Mechanics* and Associate Editor of *Journal of Engineering Mechanics* and *International Journal of Biomedical Imaging*. He is Fellow of AAAS and ASCE-EMI.